Local Relative Density Modulates Failure and Strength in Vertically Aligned Carbon Nanotubes

Siddhartha Pathak,[†,∥,*] Nisha Mohan,[†] Elizabeth Decolvenaere,[†] Alan Needleman,[‡] Mostafa Bedewy,[§] A. John Hart,[§,⊥] and Julia R. Greer[†]

[†]Materials Science, California Institute of Technology (Caltech), Pasadena, California, United States, [‡]Department of Materials Science and Engineering, College of Engineering and Center for Advanced Scientific Computing and Modeling (CASCaM), University of North Texas, Denton, Texas, United States, [§]Mechanosynthesis Group, Department of Mechanical Engineering, University of Michigan, Ann Arbor, Michigan, United States, [∥]Center for Integrated Nanotechnologies, Los Alamos National Laboratory, Los Alamos, New Mexico, United States, and [⊥]Department of Mechanical Engineering, Massachusetts Institute of Technology, Cambridge, Massachusetts, United States

ABSTRACT

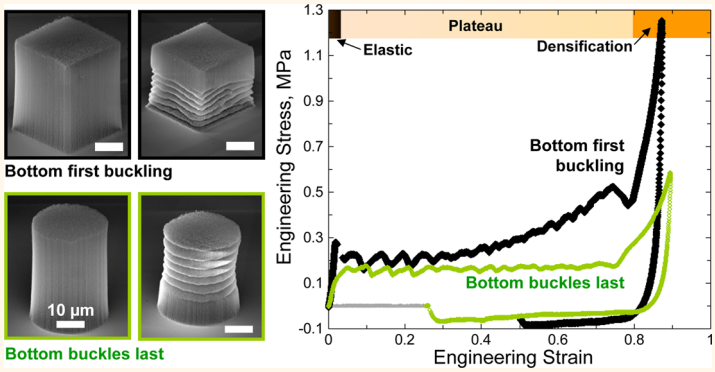

Micromechanical experiments, image analysis, and theoretical modeling revealed that local failure events and compressive stresses of vertically aligned carbon nanotubes (VACNTs) were uniquely linked to relative density gradients. Edge detection analysis of systematically obtained scanning electron micrographs was used to quantify a microstructural figure-of-merit related to relative local density along VACNT heights. Sequential bottom-to-top buckling and hardening in stress–strain response were observed in samples with smaller relative density at the bottom. When density gradient was insubstantial or reversed, bottom regions always buckled last, and a flat stress plateau was obtained. These findings were consistent with predictions of a 2D material model based on a viscoplastic solid with plastic non-normality and a hardening–softening–hardening plastic flow relation. The hardening slope in compression generated by the model was directly related to the stiffness gradient along the sample height, and hence to the local relative density. These results demonstrate that a microstructural figure-of-merit, the effective relative density, can be used to quantify and predict the mechanical response.

KEYWORDS: vertically aligned carbon nanotubes · compression · mechanical properties · energy storage · finite element simulation

Developing low-density materials for engineering applications requires a precise knowledge of relationships between their component geometries and the physical and mechanical properties of the constituent materials, like density and strength. In a typical metal, the Hall-Petch effect[1,2] relates the yield strength, σ, to the average grain size, d, through $\sigma \sim d^{1/2}$. In cellular materials, Young's modulus, E, and strength, σ, scale with density: E, $\sigma \sim \rho^{2}$.[3] Such relationships are challenging to obtain for complex hierarchical cellular structures like vertically aligned carbon nanotubes (VACNT) forests, with possible applications ranging from microelectro-mechanical systems (MEMS) to energy dissipative systems.[4−9] These materials represent examples of spatial hierarchy because the individual nanotubes have diameters on the order of tens of nanometers; the intertube distances may range from a few to hundreds of nanometers; the heights of the forests may be as high as hundreds of micrometers to several millimeters; and their lateral extent can have macroscopic dimensions. The

* Address correspondence to pathak@caltech.edu, siddharthapathak@gmail.com.

Received for review May 29, 2013 and accepted September 3, 2013.

Published online September 03, 2013
10.1021/nn402710j

complexity associated with the structure of VACNTs, as well as the unique properties driven by the nanometer dimensions and the van der Waals interactions among the individual tubes, render quantifying their physical properties like density, characteristic mean-free path, and cell size particularly challenging. No quantitative theory exists which can predict the mechanical response of carbon nanotube networks as a function of their local microstructural attributes like density, porosity, and tortuosity. Establishing such a link will serve as the foundation for predicting failure, *deformation mechanisms*, and *macroscale* mechanical properties as a function of the controllable material characteristics.

The details of VACNT synthesis[10−12] determine the diameter and quality of individual CNTs, as well as their alignment and density within the forest. Such variations are evident at the individual tube level (diameters varying between 2−3 nm,[13] to 20−50 nm,[14] to greater than 100 nm[15]) and at the collective matrix levels (density varying from 0.018[16] to 0.95 g/cm^3).[13] This is evidenced, in part, by the wide range of mechanical properties reported for VACNTs grown by different methods. For example, compressive modulus and buckling strengths of VACNTs have ranged from sub-MPa[9,17] to tens of MPa[18−20] to GPa[13,21] (Figure S1). Further, nominally identical VACNT samples have been found to both substantially recover their shape after large compressions (Figure S1a,c[4,8,9,22,23]), as well as to deform permanently even at modest strains (Figure S1b,d[14,20,24−26]).

Uniaxial compression experiments on VACNT samples with micrometer dimensions[4,10,14,23,27] and indentations into VACNT forests[13,28−30] have demonstrated their mechanical deformation characteristics to be similar to open-cell foams.[3,31] In the spirit of a foam-like response, the compressive stress−strain relationship for VACNTs has three distinct regimes: (1) initial linear elastic loading, (2) an oscillatory plateau, where each undulation in the data corresponded to a localized buckle formation in the material, and (3) a densification, manifested by a rapid stress increase. In contrast to cellular foams, which typically deform by bending and collapsing of cell walls,[3,31] postelastic flow in VACNTs is accommodated by the formation of localized folds or buckles of the entangled arrays, usually oriented orthogonally to the compression direction (Figure S1).[4,10,17,24,25,28,31] Most VACNT structures, including patterned micropillars, have been reported to follow a particular bottom-to-top buckling sequence under uniaxial compression. The first fold generally nucleated close to the substrate, and each subsequent lateral collapse event initiated only after the preceding one was completed, sequentially collapsing the entire structure.[4,10,14,23] Another departure in the compressive behavior of VACNTs from that of typical open-cell foams is that the plateau in their stress−strain curves has a positive global slope, ranging from 0.5 to 12 MPa[4,10,14,23] (Figure S1), while in open-cell foams, this plateau is virtually horizontal.[3] It has been speculated that the observed nonzero plateau slopes in VACNTs may be uniquely related to a gradient in the material mechanical properties, like stiffness or yield strength, along the sample height.[4,14] This reasoning is partly motivated by the numerous observations of localized folds within CNT structures always forming first at the locations close to the growth substrate, which correspond to the lowest CNT number density.[32,33] Sparser-spaced individual tubes close to the growth substrate reduce the load-bearing capacity of the overall structure under compression hence resulting in a lower stiffness and yield stress at the base.[4,24]

Interactions between adjacent CNTs have been investigated at molecular levels,[34−36] as well as for arrays of CNTs.[37−40] Recent computational models, which qualitatively captured the mechanics of VACNT deformation, have provided a physical foundation for strengthening in the stress plateau. Using a constitutive hardening−softening−hardening model with plastic non-normality, Hutchens *et al.*[41−43] showed that a linear variation in the input yield-like property along sample height correlated with the output slope of the stress plateau. A constant property along the sample height resulted in a flat stress plateau. Introducing a linear gradient in the input property caused a corresponding linear increase in the slope of the stress plateau. What remains unknown is the relationship between this yield-like mechanical property and physical attributes of the material. This is due, in part, to the difficulty of quantifying local microstructural characteristics of VACNTs, as well as by the lack of experimental data that show a flat plateau in the compressive stress−strain response of VACNTs.

This line of reasoning suggests that the stress−strain response of VACNT forests is related to the variations in relative density along the forest height. The development experimentally informed quantitative models of VACNT deformation has been hampered by challenges in measuring local CNT density within a forest. During the early growth of a VACNT forest, the van der Waals attraction between CNTs causes them to self-align after attaining a threshold density,[32,44] which results in the formation of a highly intertwined, porous three-dimensional network. These morphological complexities result in several challenges when using scanning electron microscopes (SEMs) to image VACNT forests: (1) ample adjustments in imaging conditions like depth of field, contrast, and brightness are required as the beam is rastered along the sample; (2) interaction volume between incident and secondary electrons is ambiguous, which obscures the interpretation of a two-dimensional image onto a three-dimensional structure; and (3) sample-to-sample variation is substantial. While other nondestructive techniques, such as small-angle X-ray scattering (SAXS) and mass attenuation,

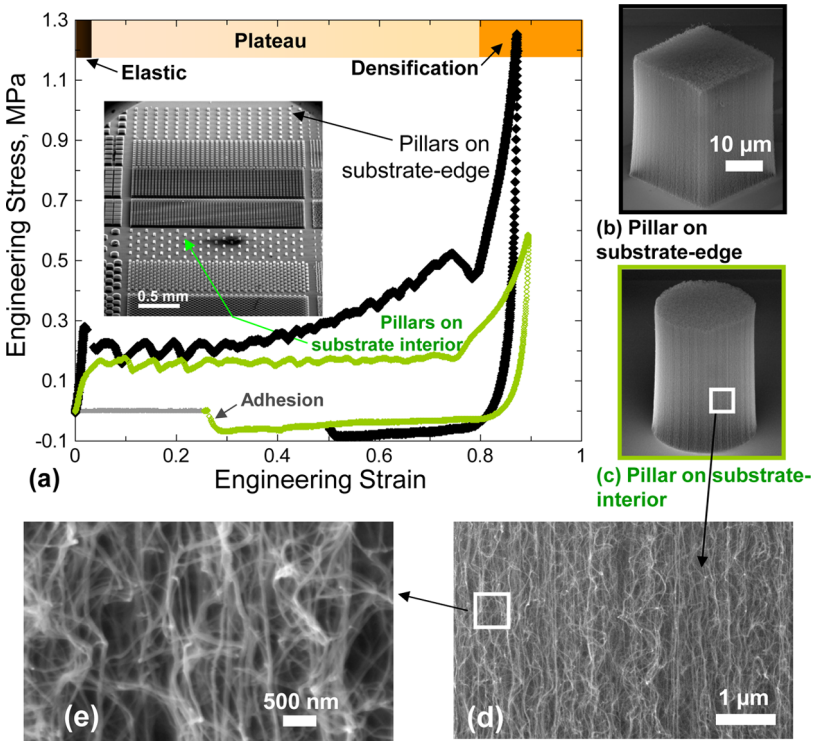

Figure 1. (a) Comparison of the stress−strain responses of two VACNT pillar systems grown on the same substrate; while the (square) pillars situation at the edge of substrate in (b) show a heavily sloped plateau region, the same for the (circular) pillars located in the interior of the substrate shown in (c) is almost flat (as in open-cell foams). The pillars on the substrate-edge also show a lower recovery than the ones on the substrate interior. Micrographs in (d) and (e) reveal the hierarchical morphology of VACNTs, which consist of nominally vertical aligned and highly anisotropic CNTs at low magnification (d), and a complex, nearly isotropic, intertwined network at higher mag (e). SEM pictures were taken at a 60° tilt angle.

have been used to quantify the evolution of alignment, diameter, and density of CNTs during growth,[32,44−46] the lower resolution and larger beam size of these techniques (>10 μm[44,47]) limit their applicability for microscale density gradient determination. Although measurements of optical extinction have been recently employed to verify density variations across individual CNT pillars,[48] we were unable (logistically, and because of sample design) to apply it to this study. Hence, we apply an edge detection technique based on the Canny algorithm[49] to systematic SEM images of VACNTs to calculate the relative differences in two-dimensional areal density as a function of spatial coordinates. A combination of image analysis, *in situ* microcompression experiments, and theoretical modeling used in this work revealed a quantifiable relationship between the relative density within VACNTs, their microstructural deformation mechanism, and the stress−strain response.

RESULTS

Compression Results. Experiments were performed on two sets of VACNT micropillars, both grown by the same chemical vapor deposition (CVD) synthesis on the same Si substrate but located on different regions of the substrate (see Methods and Figure 1). One set of VACNT micropillars was located close to the substrate edge. These samples are referred to as "pillars on substrate edge" (Figure 1b). The second set was located in the substrate interior, where they were fully surrounded by patterned VACNTs. These samples are referred to as "pillars on substrate interior" (Figure 1c). Representative compressive mechanical response of each pillar type is shown in Figure 1a. Stress−strain data for both pillar types exhibited three distinct regimes: (1) linear elastic loading, followed by (2) an oscillatory plateau extending to the strains of ~75−80%, and (3) densification, characterized by a steep stress increase upon further compression. The post-elastic stress plateau for both sets of pillars contained undulations, each of which corresponded to the consecutive buckling-like folding events (video S1 in SI). Several key differences between the two VACNT pillar types are apparent. Samples on substrate-interior had a nearly flat plateau (slope ~ 0.02 MPa) up to a strain of 75% (Figure 1a). The stress plateau in the pillars on substrate-edge had two separate slopes: a relatively flat section up to 30% strain and a steeper region, with the slope of 0.65 MPa up to unloading at 75% strain (Figure 1a). These differences in the stress plateaus between the two pillar types correlate with the stiffness change calculated from the initial unloading slope in stress−strain data (Figure S8a). The unloading stiffnesses for pillars on substrate-interior remained virtually constant when unloaded from within the stress

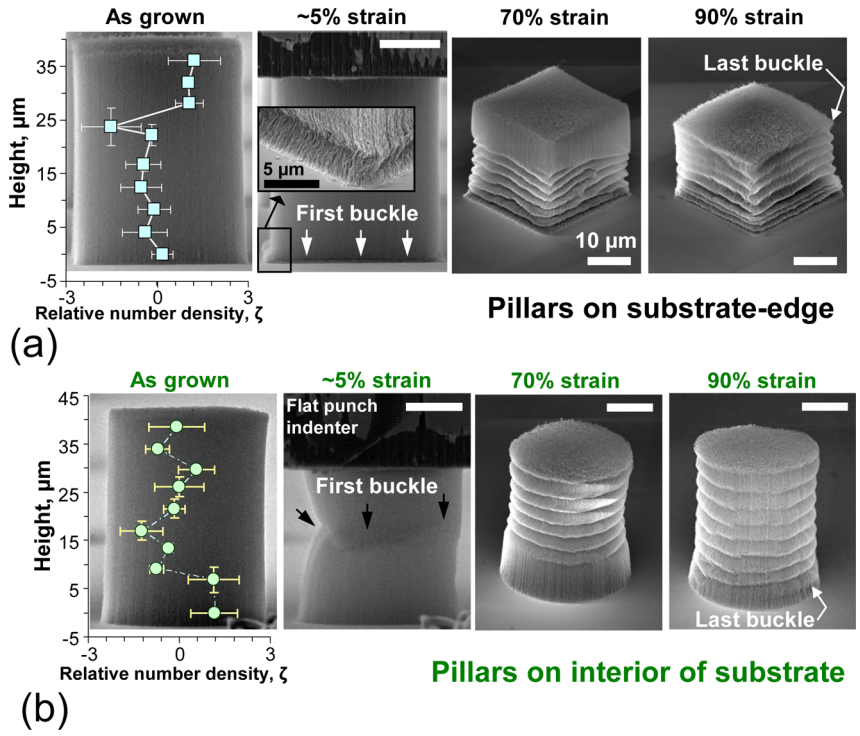

Figure 2. Relationship between the relative tube number density ζ, eq 2, and the sequence of buckle-formation for the (a) pillars on substrate-edge and (b) on interior of substrate. In (a), the pillars located on substrate-edge have a higher relative density ζ toward the top ~10 μm of the pillar, and buckles in this region of the pillar are the last to form. Buckling in these pillars follows a bottom-to-top sequence as shown by the SEM images. Thus, the first buckle always forms at the bottom (indicated by white arrows), but the top half of the pillar is still undamaged when the sample is unloaded from a strain of $\varepsilon \sim 0.7$. The top buckles (in the region with the highest ζ values) are the last to form. On the other hand, in (b) the highest values of ζ are at the bottom ~10 μm of the pillars located in the interior of the substrate. Thus, while the first buckle forms at the center for these pillars, where the ζ value is low (indicated by the black arrows), the buckles at the bottom are the last ones to form at high strain levels ($\varepsilon \sim 0.9$), *i.e.*, in the densification regime. At lower strains ($\varepsilon \sim 0.7$), the bottom section of these pillars are still free of buckles. The two left SEM images in (a) and (b) were taken at a 86° tilt angle and have the same magnification, while the two right SEM pictures (of similar magnification) were taken at a 60° tilt angle. All scale bars are of 10 μm length.

plateau region (E = 9.11 ± 2.7 MPa). Stiffness of the pillars on substrate-edge increased from $E \approx 20$ MPa to $E \approx 31$ MPa as the strain increased beyond 30%. In general, pillars on substrate-edge appeared stiffer than pillars on substrate interior (see Figure S8a). The two pillar sets also differed in the amount of recovery when unloaded from postdensification regime: pillars on substrate-interior ($R \approx 57.9 \pm 0.9\%$) showed an almost 45% higher recovery than those on substrate-edge ($R \approx 39.8 \pm 3.9\%$, Figure S8b).

In situ uniaxial compression experiments on the two sets of VACNT samples conveyed that the sequence in the localized folds formation was unique for each sample type (Figure 2). The first buckling-like instability, which corresponded to the transition from elastic loading to plateau in the stress−strain data, always formed at the bottom of the sample in the pillars on substrate-edge. After initiation, the fold propagated laterally until it fully spanned the pillar width. Bottom-to-top buckling occurred in succession, with each subsequent buckle initiating only after the previous one, located below it, had completed, similar to the observations in refs 4 and 14. Unloading from maximum compression of ~70% strain left the top third of the pillar relatively undeformed (Figure 2a, third panel from left), and the buckle closest to the top always formed last (Figure 2a, right-most panel). In contrast, SEM images of the postcompression substrate-interior pillars, unloaded from the same maximum strain of 70%, showed that it was the *bottom* third of the pillar that remained relatively undeformed (Figure 2b, third panel from left). The first instability in pillars on substrate-interior always formed somewhere at their mid-height (Figure 2b, second panel from left), and the buckle closest to the substrate always formed last (Figure 2b right-most panel). Unfortunately, the entire *in situ* deformation of pillars on substrate-interior could not be continuously visualized because their central position on the substrate prevented unobstructed observation of their compression.

DISCUSSION

Deformation Mechanism as a Function of Local Density Variation. Changes in VACNT syntheses are known to cause wide variations in their mechanical properties (see Figure S1). To avoid synthesis-induced variations, all samples in this work were physically located on the same Si substrate and were synthesized using the

same CVD process during the same run. Differences in their mechanical response, therefore, must stem from the specific details of their microstructure.[8,9,14] Hierarchical arrangements within VACNT microstructure across multiple length scales are shown in Figures 1b–e. At the lower magnifications of 4000×, sample cross sections appear either square (Figure 1b) or circular (Figure 1c). Increasing magnification 10 times to 40000× reveals the nominally vertical alignment of CNTs growing perpendicularly to the substrate within the overall VACNT network (Figure 1d). A further 5-fold increase in magnification to 200000× reveals an isotropic CNT network with significant intertwining among the somewhat vertically aligned long, curved segments of individual tubes (Figure 1e).[14,43,50] As-grown, some tube segments within the CNT forest were bent and formed contact points with other segments as a result of van der Waals forces during growth. The overall properties of such a hierarchically composed material are expected to be a combination of the mechanical attributes of its constituents at each relevant length scale; from individual nanotubes, whose properties are a function of their geometries, number of walls, and chirality, to micrometer-sized "cell" dimensions, and to the final macroscopic, monolithic-like forests. The shapes of VACNT pillar cross sections (square *vs* circular) did not appear to influence their deformation characteristics; pillars with both cross-sectional geometries showed an equivalent mechanical response and similar buckling sequences when they were located in the substrate interior (Figure S9). Thus, the substantial differences in the deformation and mechanical properties between the two pillar types studied in this work were likely caused by their differing microstructural features rather than cross-sectional shapes.

Quantification of Local Density *via* Image Analysis. Quantifying absolute density while concurrently capturing local fluctuations in density of VACNTs is challenging because these samples do not have enough mass for the standard BET-type absorption techniques[51−53] and are too complex for the typical image-based methods.[54,55] To overcome these difficulties, we chose to evaluate the *relative* changes in the local VACNT density as a function of height rather than to attempt to compute the absolute densities. We utilized edge detection techniques using the Canny algorithm[49] to systematically calculate the average relative number density, ζ, of tubes in each SEM image (see Methods). Image analysis revealed that the two types of pillars exhibited opposite trends in relative density (Figure 2a,b). Pillars on substrate-edge had highest ζ in the top 10 μm, and their density profiles resembled a step function, where $\zeta \approx 1$ for all locations above the height of ~23 μm, and $\zeta \leq 0$ at all locales below. Maximum ζ in pillars on the substrate-interior was located in the bottom ~10 μm, close to the substrate, and any changes in density within this region did not exceed the measurement error. Image analysis also revealed that the apparent density decreased in the midsection of all samples: at ~23.7 ± 3.5 μm in 36 μm tall pillars on substrate-edge and at ~16.3 ± 1.5 μm in 40 μm tall samples on substrate-interior.

Quantifying relative density differences between the two sample sets is useful in understanding their deformation mechanisms, and the knowledge of the relative density profiles can be used to predict the location of initial buckling instability in a VACNT matrix. It is reasonable to expect the first folding/buckling event during compressions of VACNTs to originate close to the substrate because of its rigid constraint.[24] Pillars located on substrate-edge corroborated this notion (Figure 2a). In contrast, the incipient instability in pillars on sample-interior occurred somewhere in the middle of pillar height, at the locales with the lowest relative CNT density. It appears that the lower relative density trumps the constraining effects of the substrate in driving the location of the buckling instability in these sample-interior pillars. The last buckles in both sets of pillars occurred in the regions with the highest relative CNT densities: near the top in the substrate-edge samples and at the base in the substrate-interior ones.

We note two important limitations associated with the calculation of ζ using eq 2 (see Methods and Figure S6): (i) the reported values of ζ may be an underestimate, because eq 2 cannot differentiate between the edges of individual CNTs and CNT bundles; (ii) possible differences in tortuosity (alignment) of the CNTs are also unaccounted for by our approach. Thus, we emphasize that the relative density profiles described in this work are indicative of the "feature" density within each individual pillar, and that comparisons of the absolute density between different pillars is not possible due to the hierarchical structure and variations in alignment between the pillars.

Previous studies have revealed that key attributes (*e.g.*, diameter, alignment, and number density) of the CNT forest morphology evolve in concert during the successive, mechanically coupled stages of growth.[32,44,46,56] These reports showed that a higher areal density of CNTs in as-grown forests results in a higher alignment, where alignment is typically quantified using an orientation parameter. Another factor that determines the tortuosity of CNTs is the stiffness of individual CNTs, which depends on both the diameter and the number of walls. Hence, growth recipes that produce higher CNT nucleation density result in denser and more aligned CNT forests, which in turn typically have greater mechanical stiffness. In addition, tuning the size of the catalyst nanoparticles seeding the growth of CNTs to favor the growth of larger diameter CNTs having more walls also produces stiffer and more aligned forests, owing to the increased stiffness and straightness of individual CNTs. We suggest that more tortuous

CNTs, which exist in lower density forests, have more defects due to the mechanochemical nature of growth,[56] which in turn may influence the mechanical properties of the forest.

Linking Density and Strength. Quantifying the local variations in density along sample heights can also be useful in predicting their compressive strengths as a function of deformation. Some of the features associated with the inelastic deformation of VACNTs under compression, that is, sequential buckle formation and plateau-densification in the stress–strain response, have been qualitatively captured using a finite deformation model by Hutchens et al.[41–43] This formulation uses a compressible elastic-viscoplastic constitutive relation with plastic non-normality and a linear hardening–softening–hardening flow strength function (see Methods). The analyses in ref 43 also showed that an axial gradient in the yield-like property over sample height correlated with the global slope in the computed stress–strain output and affected outer surface displacement. Extending this model toward mechanical stresses and strain predictions as a function of microstructural detail such as density requires determining the relationship between the relative density and a mechanical property, which corresponds to the input strength multiplier, SM, in the finite element model. For example, the $E \sim \zeta^2$ relationship for open-cell foams[3] may not hold for VACNTs, whose complex hierarchical makeup, as well as friction and van der Waals attraction among individual nanotubes, elicit a unique stress–strain response. It is reasonable to expect that the stiffness or modulus of VACNT forests would depend on the number of intertube junctions in the matrix, as well as by the number of load-bearing members and their individual mechanical properties. To determine the dependence of Young's modulus on a morphology-governed figure of merit, Astrom *et al.*[57] applied a modified semitheoretical version of the Cox shear-lag model[58] to CNT mats and fibers, while taking into account the statistical number of bundle–bundle contacts, which can be altered by chemical or irradiation-induced cross-linking. They reported that the effective modulus of a single walled CNT mat was linearly related to the average number of bundle–bundle contacts per bundle, which has not been experimentally quantified. The number of fiber crossings increased with the greater number of fibers,[59] and hence with the density, although this effect was not necessarily linear. This suggests that, to a first approximation, the stiffness of VACNTs may be linearly related to its density, $E \sim \zeta$. Such a linear correlation was experimentally verified by Bradford et al.[16] who used a postgrowth CVD treatment on VACNT arrays to systematically vary their densities and then measured compressive stresses as a function of compressive strain. Unloading elastic moduli as a function of density inferred from data reported in ref 16 shows a nearly linear E *vs* ζ dependence. This line of reasoning and a lack of any other conclusive experimental reports on the subject[30,60–62] suggests that the relationship between stiffness and relative density in VACNTs is linear.

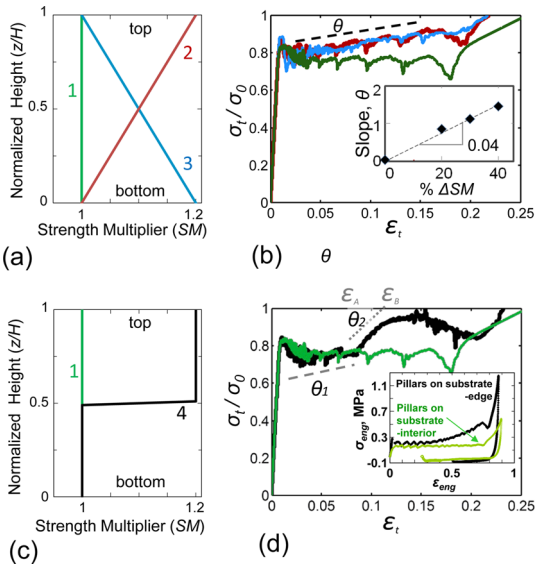

Figure 3. (a) Three variations of the SM function used for simulations: case 1, constant SM function (green curve); cases 2 and 3, linearly increasing (red curve) and decreasing (blue) SM functions respectively. (b) Corresponding normalized stress–strain curves for cases 1–3 showing a linear elastic region, buckling perturbations in the plateau region and densification at $\varepsilon_t \sim 20\%$. Inset: Plot of the hardening slope of the plateau region (θ) *vs* % ΔSM over the height of the pillar, showing a linear relationship. (c) Comparison of case 1 (green curve) *vs* case 4 (step variation of the SM function over the pillar height, black curve). (d) Corresponding normalized stress–strain curves for these two cases. Note that the plateau region in case 4 can be further subdivided by two distinct slopes, θ_1 and θ_2. (d inset) Experimental uniaxial stress–strain curves responses of the substrate-edge *vs* substrate-interior pillars showing the similarity in their responses as compared to the two simulation cases in (c).

Modeling Stress *vs* Strain with Varying Property Gradients and Elastic–Softening–Hardening Constitutive Relation. We examined the stress *vs* strain generated by the FE model, with an input constitutive relation using the same variation in SM as the variation in the relative CNT number density estimated from image analysis. We assumed that the same spatial variation holds for the modulus, E, and for reference flow strength σ_0. We explored four distinct cases: case 1, SM is constant throughout the pillar height, case 2, SM increases linearly with pillar height, case 3, SM decreases linearly with pillar height, and case 4, SM has a step-increase at the midpoint of the pillar height, that is, at $z/H = 0.5$, where z is the coordinate along the pillar height. The absolute coefficient in the linear relation between density and mechanical property will affect the linearly varying SM cases (cases 1–3, Figure 3) but is not critical when SM variation is a step function (case 4).

Strength gradients over the height in terms of SM for all four cases considered are shown in Figures 3a, c,

and normalized stress−strain data for Cases 1−3 are shown in Figures 3b and d. These plots revealed a direct linear relationship between the global hardening slope, θ, of the stress plateau and strength multiplier range ΔSM ($\Delta SM = |SM_{top} - SM_{bottom}| = 20\%$ (inset in Figure 3a). Comparing cases 2 and 3 revealed that a forward or reverse gradient in SM of the same magnitude led to the same hardening plateau slope in the normalized stress−strain curve. This lack of sensitivity to the direction in the gradient is likely due to the identical fixed boundary conditions in axial direction (but not necessarily in the radial direction) at both ends of the sample in the model. When gradients of opposite signs are prescribed, the deformation would commence in the direction of weaker-to-stronger part of the pillar, that is, in the opposing directions. No distinction between stress−strain outputs would be expected because in both cases the stress is governed by the strain rate wave overcoming the progressively harder regions, regardless of their position within the pillar. For case 4, where SM is represented as a step function along the sample height and which matches the experiment most closely, a single value of slope was insufficient to characterize the stress−strain data. Two distinct slopes, θ_1 and θ_2, correlated with the relatively porous (weaker) bottom part and the more densely populated (stiffer) top segment. The normalized stress−strain curve for case 4 (Figure 3d, black curve) closely matched that for case 1 (constant property, no gradient) until ε_A. The second slope, θ_2, between the strains of ε_A and ε_B, was significantly higher than θ_1 due to the abrupt shift to higher strengths in the middle of the pillar. The hardening slope in case 1, uniquely defined by a single value of θ, was lower compared to the two linearly varying cases (cases 2 and 3), which suggests a linear relation between output slope θ and input property variation, ΔSM. In all cases, the slope(s) of the stress−strain output generated by the FE model qualitatively reflected the shape of the input yield-like property gradient. It is reasonable that this linear correlation can provide a quantifiable link between the measurable microstructural property, density, and macroscopic mechanical response, that is, stress, as a function of strain.

Table 1 provides a matrix of input and output parameters for each studied case. Additional output figures of merit were amplitude, a, and wavelength, λ, of the outer surface displacement undulations, whose definitions are schematically shown in Figure 4a. Table 1 demonstrates a close-to-50% drop in the amplitude of oscillations in case 3 (negative property gradient) compared to case 1 (no gradient), likely due to the substrate-like hindrance from the fixed radial displacement boundary condition at the bottom. As the instability progresses from the top toward the bottom of the sample, radial displacements are restricted, which lowers the buckle amplitude.

TABLE 1. Comparison of the Deformation Characteristics Measured for the Four Variations of the SM Function

case #	slope	transition strain	buckle amplitude (Ur/R)	buckle wavelength (λ/R)
1	$\theta = 0.037$	$\varepsilon = 0.155$	0.022	0.092
2	$\theta = 0.862$	$\varepsilon = 0.155$	0.022	0.094
3	$\theta = 0.853$	$\varepsilon = 0.17$	0.014	0.086
4	$\theta_1 = 0.025$	$\varepsilon_A = 0.089$	0.013	0.043
	$\theta_2 = 3.6$	$\varepsilon_B = 0.126$		

The buckle wavelength remained unaffected because the axial boundary conditions at the top and bottom were similar. The presence of a step-shaped barrier in strength in case 4 reduces the effective length of pillar to half of its real length, allowing only the lower half to undergo sequential folding, while the upper half has a single instability. In this case, both the amplitude and the wavelength of the outer surface displacements were lower than in all other cases. Assuming a linear correlation between the local density and yield-like strength at the same location, strength variations in the simulated cases 1 and 4 represent reasonable approximations to the density distributions gleaned from the uninformed image analysis for the two sets of pillars. Both experimental and simulated stress *vs* strain relationships reflect the attributes of these input variations.

Effects of Strain Rate Wave. We also evaluated the effects of strain rate within the individual folding events. The folding instability appears to occur in two consecutive phases: initiation and propagation. The initiation of these instabilities is uniquely defined by and is sensitive to the direction of the density gradient: the first fold/buckling-like instability always nucleated at the weakest point over the height. This holds true in both the experiment (Figure 2) and the simulations (Figure 3). For case 2, where SM function is lowest at the bottom of the pillar, the first buckle occurred at the pillar base, while the reverse holds true for case 3, which had the lowest SM value at the top of the sample. Case 4 in the simulations differed from all others because the sequential buckling propagated only in the relatively weaker bottom half of the pillar. The hardening slope θ_1 from the initial loading to ε_A for case 4 (step function) was virtually equivalent to that for case 1 (uniform property), which implies that the strain rate wave had not yet reached the strength barrier at that point (see Table 1). Figure 4a shows outer surface displacements for each studied case at four progressively higher applied strains, and Figure 4b shows the strain rate contour plots within the buckling phases for the no-gradient case (case 1). These computational results revealed that in case 1 (no gradient) the first fold initiated at the bottom with a localized increase in strain rate, which initiated at the onset of the first buckling instability (leftmost panel in Figure 4b) and propagated laterally to the right while

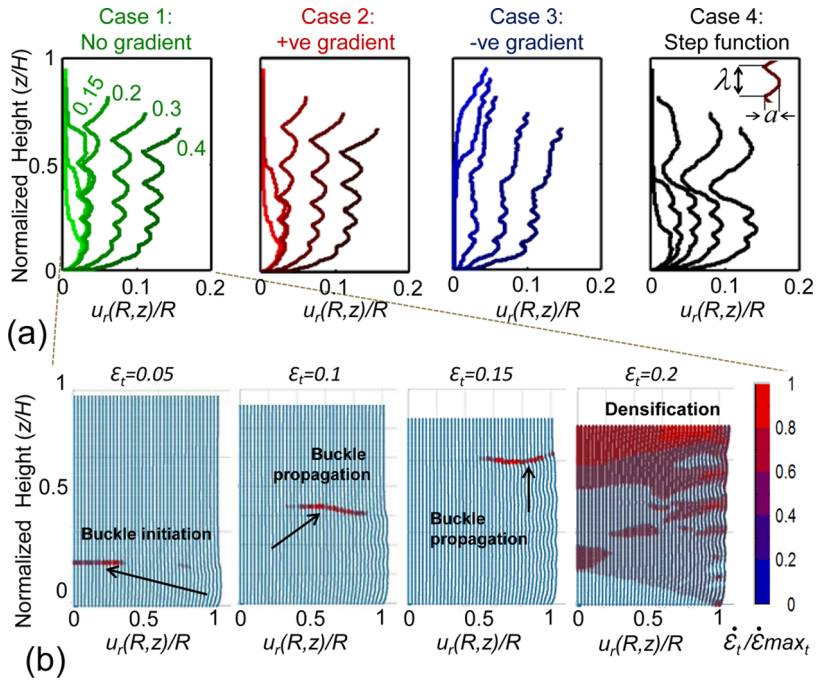

Figure 4. (a) Simulation results showing the evolution of the outer deformation profiles corresponding to the four different SM functions shown in Figure 3. The profiles are shown for strains of 5, 10, 20, 30, and 40%. Case 1 also shows an extra profile at 15% strain. (b) Strain rate contour plots for case 1 at four consecutive strains showing buckle initiation (ε_t = 0.05), propagation (ε_t = 0.1 and 0.15), and densification with high strain rate distribution (ε_t = 0.2). The contour of high strain rate, which originates at the bottom right corner of the pillar due to restrictive boundary conditions, propagates sideways and also climbs the pillar height simultaneously. Further buckles initiate sequentially in the section below this wavefront.

concurrently progressing toward the top (Figure 4b, second and third panels). At each strain, only the part of pillar below the strain rate wave buckled, which led to the sequential formation of folds as the wave propagated through the structure. When the wave reached the top of the pillar, the plastic strain in the entire sample shifted the response into the densification phase. This was indicated by the increased strain rate in the entire sample (the rightmost panel of Figure 4b) and the steep increase in the normalized stress at strains greater than ε_t = 0.2 (Figure 3d).

CONCLUSIONS

The combination of microcompression experiments on VACNTs cylinders, edge detection analysis of their images, and mechanical modeling revealed that the commencement of local failure events and compressive stress–strain responses were uniquely linked to relative density gradients. Two nominally identical sets of VACNT samples exhibited distinct commencement of local failure events and dissimilar mechanical response under compression. Edge detection analysis of systematically obtained SEM images uncovered that these differences in failure location and attained strengths were driven by the relative local density variations along the sample height. Samples with a lower density at the bottom of the forest compressed by forming sequential buckling-like folds, which emanated from the bottom and propagated toward the top. When the density gradient was insubstantial or reversed, the bottom regions always buckled last. Two-dimensional, local material model based on a visco-plastic solid with plastic non-normality and with the effective stress–strain relation containing an initial peak, softening and hardening revealed that the hardening slope of compressive stress plateau was directly related to the gradient in stiffness, and hence, local relative density, along the pillar height. Results of this work demonstrate that a controllable microstructural figure of merit (*i.e.*, relative density) can effectively represent this complex microstructure, which can then be used to quantify and predict mechanical failure.

MATERIALS AND METHODS

CNT Pillar Growth. VACNTs were synthesized by catalytic CVD in a hot-walled reactor (Thermo-Fisher Mini-Mite, 22 mm inner diameter tube furnace with 12 in. heated length), from substrate-bound catalyst nanoparticles. Substrates were prepared by the physical vapor deposition of 1 nm of iron after 10 nm of alumina on a thermally oxidized (100) silicon wafer (0.5 mm thick). Micron-sized CNT pillars were prepared by photolithographic patterning of catalyst deposition (using SPR-220–3 photoresist). After lift-off of photoresist, centimeter-sized silicon chips were loaded inside a quartz tube within the tube furnace. Before introducing the growth gas (ethylene) into the reactor, the multilayer thin film catalyst was heated in an atmosphere of hydrogen/helium to induce film dewetting into nanoscale

particles. LabVIEW was used to interface and control all process variables, such as temperature and gas flow rates. After a 5 min helium (1000 sccm) purging step, hydrogen (400 sccm) and helium (100 sccm) were mixed and the temperature was ramped up to 775 °C for 10 min. The same temperature was maintained for another 10 min. Finally, ethylene (100 sccm) was introduced to the system for a maximum of 30 growth minutes. After growth, the tube was purged again with helium during cooling.

***Ex Situ* Compression Experiments.** Two sets of stand-alone patterned VACNT samples, grown on the same Si substrate, were chosen for the compression tests (see Figures 1 and S9). While both sample sets were patterned as micropillars, their locations on the substrate significantly affected their mechanical response. One set of VACNT micropillars was located at the edge of the substrate and had square cross sections with side lengths of ~25 μm (referred to as "pillar on substrate edge", Figures 1b and S9). This set consisted of three rows of pillars at the extreme edge of substrate (a total of 51 pillars, three rows of 17 pillars each). All remaining pillars were located in the interior of the substrate where it was surrounded by patterned VACNTs on all sides. The VACNT micropillars in this set includes the remaining square pillars, which were situated in a more interior location (Figure S9c), as well as the pillars with circular cross sections with diameters of ~28 μm (referred to as "pillar on substrate interior", Figures 1c and S9). A total of 114 pillars tested showed the "pillars in substrate interior" behavior, out of which 34 were pillars of square cross section and the rest of circular cross section. The heights of both types of samples increased from 30 to 40.5 μm for the edge and from 38.7 to 42.6 μm for the interior samples over the lateral distance of 2 mm on the Si substrate.

The compression experiments were performed in air, using the XP module of Agilent's nanoindenter G200 with a custom fabricated, ~120 μm diameter, diamond flat punch indenter tip. Tests were performed at constant displacement rates of 10, 100, and 1000 nm/s using the Testworks software control methods described in ref 14. The maximum prescribed displacements ranged from 10 to 90% of the pillar heights, with multiple (up to 99) unload–reload cycles performed on the same pillar at discrete displacement intervals. During cyclical testing, the samples were unloaded to 10% of the maximum load in the previous cycle and immediately unloaded (i.e., no hold segments). At least five tests were conducted at each compression rate.

***In Situ* Compression Experiments.** *In situ* uniaxial compression tests were conducted to capture the local microstructural evolution in the course of deformation. The *in situ* testing was conducted in a custom built nanomechanical instrument, SEMentor,[63] which is comprised of a nanomechanical dynamic contact module (Agilent Corp.) inside of a SEM (Quanta 200, FEI). The experimental methodology was nominally identical to the *ex situ* experiments, with the exceptions of a vacuum environment and the flat punch dimensions of ~60 × 80 μm in the SEMentor. The compression axis in the SEMentor is inclined by ~86° with respect to the vertically oriented electron beam, which allows for the unobstructed view of the deforming gauge section, while simultaneously acquiring the mechanical load and displacement data. The continuously captured image scans were recorded as a video file during the test and were synchronized with the mechanical data during postprocessing to correlate each video frame with its corresponding position on the stress–strain curve (see video S1 in the SI). The CNT micropillars in the SEMentor were compressed horizontally, that is, with the gravity acting perpendicular to the compression axis, while those in the G200 were conducted vertically. Although the effects of these differences are expected to be minor, the SEMentor-generated results were limited to visualization purposes, and all the data analyses were performed on tests conducted *ex situ* in air in G200.

Data Analysis. Engineering stresses (σ) and strains (ε) were calculated using the initial dimensions of the VACNT micropillar along with the corrected load (p_{corr}) and displacement (u_{corr}) following the procedure in ref 14.

$$\sigma = \frac{p_{corr}}{A_0}, \varepsilon = \frac{u_{corr}}{h_0} \quad (1)$$

where $A_0 = w_0^2$ for the square pillars on substrate edge with the initial side width w_0, $A_0 = \pi d_0^2/4$ for the circular pillars on substrate interior with the initial diameter d_0 and h_0 was the initial height of the pillars. Frictional forces between the VACNT pillar and the indenter head were not taken into account.[64−66] The unloading modulus (E) was calculated from the initial unloading slope of the stress–strain curves. The percentage recovery (R) was defined as the strain recovered at the end of every cycle with respect to the total applied strain, $R = (\varepsilon_{max} - \varepsilon_{unload})/(\varepsilon_{max})$, where ε_{max} is the maximum strain at the end of loading and ε_{unload} is the strain after unloading to 10% of the max load in the previous cycle.

Image Analysis. The relative change in VACNT density along the heights of the samples was computed using an algorithmic image analysis technique centered on edge detection. During imaging, the samples were tilted to 30° with respect to the direction of the electron beam and imaged in a Zeiss 1550VP field emission SEM. The best imaging conditions were determined to be at 100 kX magnification, 10 kV accelerating voltage, at a working distance of 6 mm. These parameters captured a large enough representative area of the VACNT forest while maintaining an adequate resolution of the individual CNTs and bundles. To improve accuracy and to reduce variability in the interaction volume, the same SEM imaging conditions were maintained for each sample. A total of 9–10 images at evenly spaced intervals were taken along the height of each pillar. The prescribed imaging contrast was set as constant along the entire height of every sample, and only the brightness was adjusted to capture the full range of the intensity spectrum. To avoid any loss in resolution due to the 30° tilt of the samples, only the central 10% of each image was used for image analysis, as demonstrated in Figure S2.

To estimate the number of CNTs in each image, the images were first converted to grayscale, and the edges were identified and isolated using the Canny algorithm[49] (Figure S2). This method has been shown to be more accurate than the pure threshold-based methods[61] because it preserves the overlapping tubes as individual entities. The Canny algorithm is deterministic, that is, it always produces the same result for the same image, and it is not sensitive to the image brightness or its gradient. In the Canny algorithm, the image is first blurred using a Gaussian filter to remove the noise, with the pixel radius of the filter chosen specifically to minimize the background noise while preserving the necessary detail. In this work, a radius of 3 pixels, which corresponds to 1.8 nm in the SEM images, was taken as the lower bound for the width of the tubes that were in best focus, that is, likely located in the front of the sample. The partial derivatives of the intensities were taken along the horizontal and vertical directions in the image and were subsequently inserted into analytical expressions to produce sets of angles and magnitudes of these partial derivatives at each point. A total of six discrete angles were evaluated at each point to minimize both computational time and the rate of false negatives. The resulting magnitudes were further filtered by the nonmaximum suppression method,[67] which leaves only the image of the local maxima in the intensity gradient. The resulting image was thresholded based on these magnitudes, using hysteresis to preserve the neighboring lower intensity magnitudes that may belong to longer lines. Finally a black-and-white image was generated with a pixel intensity of 1 at the detected "edges", and 0 was assigned to all other locations. The resulting binary image was subsequently treated as a matrix and summed along the rows, producing a column vector of the number of edges.

Hereafter, the number of edges per unit width in each SEM image was calculated as half of the average of the column vectors. Although these values were found to be comparable across different samples captured with identical imaging conditions, the dependence of the Canny algorithm on the gradient means that the images had to be standardized for cross-comparison. This normalization required the images to be modified such that the mean became 0 and the standard deviation became 1. This was accomplished by defining the average relative CNT number density, ζ, as

$$\zeta = \frac{x - \mu}{\sigma} \quad (2)$$

where μ represents the mean number density of tubes in a set of images from a single pillar, and σ is the standard deviation of the mean number density of tubes in the same set. In eq 2, x is the pixel count transformed into a number density of tubes, that is, $x = (hw)n/2$, where n is the pixel count in the central 10% of the image, and h and w are the number of rows and columns in that region, respectively. The factor of 2 is to account for both edges of each tube. A minimum of three pillars was used to generate the data of ζ *versus* vertical coordinate for a particular category of pillar morphology.

A number of validation steps were taken to ensure both the efficacy and the repeatability of this approach. The efficacy of ζ serving as a reliable figure-of-merit was crosschecked by a manual tube-counting procedure, described in detail in Figure S3. We also ensured the repeatability of the image analysis procedures by (a) imaging the same pillar over two different SEM sessions and comparing the results (Figure S4) and (b) imaging the pillars across their width (to check for lateral variations in ζ, Figure S5). These results are detailed in the SI.

Several important limitations associated with this method exist. First, by counting edges within the image, the algorithm cannot differentiate between the individual CNTs and CNT bundles. The VACNT forest is clearly a hierarchical morphology whose mechanical properties depend not only on the CNT diameter, density, and alignment, but also on the hierarchical bundling which cannot be quantified in 3D by any known method. A difference in tortuosity of the CNTs is visually apparent when comparing representative SEM images from the two VACNT sample sets (see Figure S6), which is not accounted for in eq 2. Variations in tortuosity have been reported to significantly affect the mechanical behavior of VACNT films.[68] We emphasize that the relative density profiles described in this work are indicative of the "feature" density within each individual pillar, and that comparisons of the absolute density between different pillars is not possible due to the hierarchical structure and variations in alignment between the pillars.

Model Formulation. The mechanical behavior of the VACNT pillars with circular cross sections under compressive loading was modeled using a dynamic, axisymmetric finite element code with loading conditions aimed at modeling quasi-static response, as described in ref 43. A compressible, isotropic elastic-viscoplastic constitutive relationship with plastic non-normality and a piecewise, linear hardening−softening−hardening type of flow strength function was used to model the material. This formulation has been reported to qualitatively capture some of the characteristics of the compression of VACNT microcylinders, such as the sequential formation of localized through-thickness folds oriented orthogonally to the compression direction and the oscillatory plateau region within the stress−strain curve, where each undulation corresponds to the formation and propagation of individual instabilities.[42] The global slope of the stress plateau region, θ, was reported to correlate with the mechanical yield-like property gradient along the sample height. With plastic non-normality the flow rule is characterized by two tensors p and q, defined as $p = \tau - \beta_p \mathrm{tr}(\tau) I$ and $q = \tau - \alpha_p \mathrm{tr}(\tau) I$, with τ as the Kirchhoff stress and I as the identity tensor. In the calculations here, $\alpha_p = 0.2$, $\beta_p = 0.28$, $E/\sigma_0 = 100$ (ratio of Young's modulus to reference strength, $m = 0.02$ (rate hardening exponent), $H/R = 3$ (height to radius of pillar), $\varepsilon_0 = 5000$ (the reference strain rate). The effective flow strength function g is specified as a function of the effective plastic strain ε_p as

$$\begin{aligned} g(\varepsilon_p)/\sigma_0 &= 1 + h_1(\varepsilon_p),\ \varepsilon_p < \varepsilon_1; \\ &= 1 + h_1(\varepsilon_1) + h_2(\varepsilon_p - \varepsilon_1),\ \varepsilon_1 < \varepsilon_p < \varepsilon_2; \\ &= 1 + h_1(\varepsilon_1) + h_2(\varepsilon_2 - \varepsilon_1) + h_3(\varepsilon_p - \varepsilon_2),\ \varepsilon_p > \varepsilon_2 \end{aligned} \quad (3)$$

where σ_0 is the reference flow strength, $h_1 = 5.0$, $h_2 = -1.5$, $h_3 = 1.5$, $\varepsilon_1 = 0.005$, and $\varepsilon_2 = 0.1$. Further details of the constitutive relation are given in Needleman *et al.*[42]

In the analyses in ref 42, the mechanical property gradient was represented by a strength multiplier, SM, which is a multiplier giving the spatial variations of E (Young's modulus) and σ_0, where $SM = E/E_{bottom}$ and similarly for σ_0 (see Figure S7). In this work we further explored the effects of such a property gradient, focusing on four cases: case 1, SM is constant throughout the pillar height; case 2, SM increases linearly with pillar height; case 3, SM decreases linearly with pillar height; and case 4, SM has a step-increase at the midpoint of the pillar height, that is, at $z/H = 0.5$, where z is the coordinate along the pillar height. The range of ΔSM ($=|SM_{top} - SM_{bottom}|$ (note SM_{bottom} is necessarily equal to 1) as defined in Figure S7) was restricted to be between 0 to 40% because sequential buckling was found to disappear outside of this range.[42]

The computational results were analyzed in terms of (1) the overall pillar stress−strain response, (2) the displacement contours of the outer edge of the pillar, and (3) the strain rate distributions, all as functions of the overall pillar strain. As described in ref 36, the true stress σ_t is calculated as $\sigma_t = (P)/(\pi(R + u_r(R,H,t))^2)$, where P is the normal compressive force computed from the quasi-static principle of virtual work, and u_r is the radial displacement of the pillar at $r = R$, $z = H$, and at time t. The true stress is normalized by the reference yield stress σ_0. The true strain was computed by $\varepsilon_t = -\ln(1 + \varepsilon_n)$, with ε_n representing the nominal strain ($\varepsilon_n = \Delta H/H$), where ΔH is the top displacement, normalized by the initial height.

The computational results are compared with the experimental results in terms of (1) the transition strains (ε_A and ε_B, Figure 3d) and (2) the overall pillar hardening slope (θ) of the plateau region in the normalized stress−strain response. Cases 1, 2, and 3 required a single value of θ to define the entire plateau region, whereas in case 4 (the SM step function), the plateau region had to be subdivided into two separate regions with the individual slopes of θ_1 and θ_2 (Figure 3d). The evolution of the outer surface profiles was characterized in terms of the average amplitude (a) and wavelength (λ, Figure 4a, right panel inset) of the resulting undulations at $\varepsilon_t = 40\%$ for each studied case. The strain rate distributions (Figure 4b), which are helpful for visualizing the sequential buckling process, are shown at the strains of $\varepsilon_t = 5\%$ (initiation of the buckle-like fold), $\varepsilon_t = 10$ and 15% (propagation), and $\varepsilon_t = 20\%$ (densification) for the flat SM function (case 1).

Conflict of Interest: The authors declare no competing financial interest.

Acknowledgment. The authors acknowledge financial support from the Institute for Collaborative Biotechnologies (ICB) through Grant W911NF-09-0001 from the U.S. Army Research Office. The content of the information does not necessarily reflect the position or the policy of the Government, and no official endorsement should be inferred. S.P. gratefully acknowledges support from the W.M. Keck Institute for Space Studies Postdoctoral Fellowship program for this work.

Supporting Information Available: Video S1 illustrates the *in situ* deformation of a VACNT micropillar located on the substrate-edge when compressed at a 100 nm/s displacement rate. The online video file, synchronized with its engineering stress−strain response, is shown at 35 times its original speed. Figures S1−9 also provided. This material is available free of charge *via* the Internet at http://pubs.acs.org.

REFERENCES AND NOTES

1. Hall, E. O. The Deformation and Ageing of Mild Steel III. Discussion of Results. *Proc. Phys. Soc., London, Sect. B* **1951**, *64*, 747–753.
2. Petch, N. J. Cleavage Strength of Polycrystals. *J. Iron Steel Inst.* **1953**, *174*, 25–28.
3. Gibson, L. J.; Ashby, M. F. *Cellular Solids: Structure and Properties*; Cambridge University Press: Cambridge, U.K., 1999.
4. Cao, A. Y.; Dickrell, P. L.; Sawyer, W. G.; Ghasemi-Nejhad, M. N.; Ajayan, P. M. Super-Compressible Foamlike Carbon Nanotube Films. *Science* **2005**, *310*, 1307–1310.
5. Misra, A.; Greer, J. R.; Daraio, C. Strain Rate Effects in the Mechanical Response of Polymer-Anchored Carbon Nanotube Foams. *Adv. Mater.* **2008**, *20*, 1–5.

6. Cho, J.; Richards, C.; Bahr, D.; Jiao, J.; Richards, R. Evaluation of Contacts for a MEMS Thermal Switch. *J. Micromech. Microeng.* **2008**, 18.
7. Cola, B. A.; Xu, J.; Fisher, T. S. Contact Mechanics and Thermal Conductance of Carbon Nanotube Array Interfaces. *Int. J. Heat Mass Transfer* **2009**, *52*, 3490–3503.
8. Xu, M.; Futaba, D. N.; Yamada, T.; Yumura, M.; Hata, K. Carbon Nanotubes with Temperature-Invariant Viscoelasticity from 196° to 1000 °C. *Science* **2010**, *330*, 1364–1368.
9. Suhr, J.; Victor, P.; Sreekala, L. C. S.; Zhang, X.; Nalamasu, O.; Ajayan, P. M. Fatigue Resistance of Aligned Carbon Nanotube Arrays under Cyclic Compression. *Nat. Nanotechnol.* **2007**, *2*, 417–421.
10. Yaglioglu, O.; Cao, A.; Hart, A. J.; Martens, R.; Slocum, A. H. Wide Range Control of Microstructure and Mechanical Properties of Carbon Nanotube Forests: A Comparison Between Fixed and Floating Catalyst CVD Techniques. *Adv. Funct. Mater.* **2012**, *22*, 5028–5037.
11. Kumar, M.; Ando, Y. Chemical Vapor Deposition of Carbon Nanotubes: A Review on Growth Mechanism and Mass Production. *J. Nanosci. Nanotechnol.* **2010**, *10*, 3739–3758.
12. Presser, V.; Heon, M.; Gogotsi, Y. Carbide-Derived Carbons - From Porous Networks to Nanotubes and Graphene. *Adv. Funct. Mater.* **2011**, *21*, 810–833.
13. Pathak, S.; Cambaz, Z. G.; Kalidindi, S. R.; Swadener, J. G.; Gogotsi, Y. Viscoelasticity and High Buckling Stress of Dense Carbon Nanotube Brushes. *Carbon* **2009**, *47*, 1969–1976.
14. Hutchens, S. B.; Hall, L. J.; Greer, J. R. *In Situ* Mechanical Testing Reveals Periodic Buckle Nucleation and Propagation in Carbon Nanotube Bundles. *Adv. Funct. Mater.* **2010**, *20*, 2338–2346.
15. Qi, H. J.; Teo, K. B. K.; Lau, K. K. S.; Boyce, M. C.; Milne, W. I.; Robertson, J.; Gleason, K. K. Determination of Mechanical Properties of Carbon Nanotubes and Vertically Aligned Carbon Nanotube Forests Using Nanoindentation. *J. Mech. Phys. Solids* **2003**, *51*, 2213–2237.
16. Bradford, P. D.; Wang, X.; Zhao, H.; Zhu, Y. T. Tuning the Compressive Mechanical Properties of Carbon Nanotube Foam. *Carbon* **2011**, *49*, 2834–2841.
17. Tong, T.; Zhao, Y.; Delzeit, L.; Kashani, A.; Meyyappan, M.; Majumdar, A. Height Independent Compressive Modulus of Vertically Aligned Carbon Nanotube Arrays. *Nano Lett.* **2008**, *8*, 511–515.
18. Mesarovic, S. D.; McCarter, C. M.; Bahr, D. F.; Radhakrishnan, H.; Richards, R. F.; Richards, C. D.; McClain, D.; Jiao, J. Mechanical Behavior of a Carbon Nanotube Turf. *Scr. Mater.* **2007**, *56*, 157–160.
19. Qiu, A.; Bahr, D. F.; Zbib, A. A.; Bellou, A.; Mesarovic, S. D.; McClain, D.; Hudson, W.; Jiao, J.; Kiener, D.; Cordill, M. J. Local and Non-Local Behavior and Coordinated Buckling of CNT Turfs. *Carbon* **2011**, *49*, 1430–1438.
20. Zhang, Q.; Lu, Y. C.; Du, F.; Dai, L.; Baur, J.; Foster, D. C. Viscoelastic Creep of Vertically Aligned Carbon Nanotubes. *J. Phys. D: Appl. Phys.* **2010**, *43*, 315401–1−7.
21. Deck, C. P.; Flowers, J.; McKee, G. S. B.; Vecchio, K. Mechanical Behavior of Ultralong Multiwalled Carbon Nanotube Mats. *J. Appl. Phys.* **2007**, *101*, 23512–1−9.
22. Xu, M.; Futaba, D. N.; Yumura, M.; Hata, K. Carbon Nanotubes with Temperature-Invariant Creep and Creep-Recovery from −190 to 970 °C. *Adv. Mater.* **2011**, *23*, 3686–3691.
23. Pathak, S.; Lim, E. J.; Pour Shahid Saeed Abadi, P.; Graham, S.; Cola, B. A.; Greer, J. R. Higher Recovery and Better Energy Dissipation at Faster Strain Rates in Carbon Nanotube Bundles: An *In Situ* Study. *ACS Nano* **2012**, *6*, 2189–2197.
24. Zbib, A. A.; Mesarovic, S. D.; Lilleodden, E. T.; McClain, D.; Jiao, J.; Bahr, D. F. The Coordinated Buckling of Carbon Nanotube Turfs under Uniform Compression. *Nanotechnology* **2008**, *19*, 175704–1-7.
25. Cao, C.; Reiner, A.; Chung, C.; Chang, S.-H.; Kao, I.; Kukta, R. V.; Korach, C. S. Buckling Initiation and Displacement Dependence in Compression of Vertically Aligned Carbon Nanotube Arrays. *Carbon* **2011**, *49*, 3190–3199.
26. Yaglioglu, O. Carbon Nanotube Based Electromechanical Probes. *Ph.D. Thesis*, Massachusetts Institute of Technology, Cambridge, MA, 2007.
27. Raney, J. R.; Misra, A.; Daraio, C. Tailoring the Microstructure and Mechanical Properties of Arrays of Aligned Multiwall Carbon Nanotubes by Utilizing Different Hydrogen Concentrations during Synthesis. *Carbon* **2011**, *49*, 3631–3638.
28. Maschmann, M. R.; Qiuhong, Z.; Feng, D.; Liming, D.; Baur, J. Length Dependent Foam-Like Mechanical Response of Axially Indented Vertically Oriented Carbon Nanotube Arrays. *Carbon* **2011**, *49*, 386–397.
29. Pathak, S.; Mohan, N.; Pour Shahid Saeed Abadi, P.; Graham, S.; Cola, B. A.; Greer, J. R. Compressive Response of Vertically Aligned Carbon Nanotube Films Gleaned from *In Situ* Flat Punch Indentations. *J. Mater. Res.* **2013**, 10.1557/jmr.2012.366.
30. McCarter, C. M.; Richards, R. F.; Mesarovic, S. D.; Richards, C. D.; Bahr, D. F.; McClain, D.; Jiao, J. Mechanical Compliance of Photolithographically Defined Vertically Aligned Carbon Nanotube Turf. *J. Mater. Sci.* **2006**, *41*, 7872–7878.
31. Maschmann, M. R.; Ehlert, G. J.; Park, S. J.; Mollenhauer, D.; Maruyama, B.; Hart, A. J.; Baur, J. W. Visualizing Strain Evolution and Coordinated Buckling within CNT Arrays by *In Situ* Digital Image Correlation. *Adv. Funct. Mater.* **2012**, *22*, 4686–4695.
32. Bedewy, M.; Meshot, E. R.; Guo, H.; Verploegen, E. A.; Lu, W.; Hart, A. J. Collective Mechanism for The Evolution and Self-Termination of Vertically Aligned Carbon Nanotube Growth. *J. Phys. Chem. C* **2009**, *113*, 20576–20582.
33. Pour Shahid Saeed Abadi, P.; Hutchens, S.; Taphouse, J. H.; Greer, J. R.; Cola, B. A.; Graham, S. The Effect of Morphology on the Micro-Compression Response of Carbon Nanotube Forests. *Nanoscale* **2012**, *4*, 3373–3380.
34. Chen, B.; Gao, M.; Zuo, J. M.; Qu, S.; Liu, B.; Huang, Y. Binding Energy of Parallel Carbon Nanotubes. *Appl. Phys. Lett.* **2003**, *83*, 3570–3571.
35. Liew, K. M.; Wong, C. H.; Tan, M. J. Buckling Properties of Carbon Nanotube Bundles. *Appl. Phys. Lett.* **2005**, *87*, 041901.
36. Zhou, W.; Huang, Y.; Liu, B.; Hwang, K. C.; Zuo, J. M.; Buehler, M. J.; Gao, H. Self-Folding of Single- and Multiwall Carbon Nanotubes. *Appl. Phys. Lett.* **2007**, *90*, 073107.
37. Cranford, S.; Yao, H.; Ortiz, C.; Buehler, M. J. A Single Degree of Freedom "Lollipop" Model for Carbon Nanotube Bundle Formation. *J. Mech. Phys. Solids* **2010**, *58*, 409–427.
38. Cranford, S.; Buehler, M. J. Mechanomutable Carbon Nanotube Arrays. *Int. J. Mater. Struct. Integr.* **2009**, *3*, 161–178.
39. Fraternali, F.; Blesgen, T.; Amendola, A.; Daraio, C. Multiscale Mass-Spring Models of Carbon Nanotube Foams. *J. Mech. Phys. Solids* **2011**, *59*, 89–102.
40. Buehler, M. J. Mesoscale Modeling of Mechanics of Carbon Nanotubes: Self-Assembly, Self-Folding, and Fracture. *J. Mater. Res.* **2006**, *21*, 2855–2869.
41. Hutchens, S. B.; Needleman, A.; Greer, J. R. Erratum: Analysis of Uniaxial Compression of Vertically Aligned Carbon Nanotubes (*Journal of the Mechanics and Physics of Solids* **2011**, *59*, 2227−2237). *J. Mech. Phys. Solids* **2012**, *60*, 1753–1756.
42. Needleman, A.; Hutchens, S. B.; Mohan, N.; Greer, J. R. Deformation of Plastically Compressible Hardening-Softening-Hardening Solids. *Acta Mech. Sin.* **2012**, *28*, 1115–1124.
43. Hutchens, S. B.; Needleman, A.; Greer, J. R. Analysis of Uniaxial Compression of Vertically Aligned Carbon Nanotubes. *J. Mech. Phys. Solids* **2011**, *59*, 2227–2237.
44. Bedewy, M.; Meshot, E. R.; Reinker, M. J.; Hart, A. J. Population Growth Dynamics of Carbon Nanotubes. *ACS Nano* **2011**, *5*, 8974–8989.
45. Wang, B. N.; Bennett, R. D.; Verploegen, E.; Hart, A. J.; Cohen, R. E. Characterizing the Morphologies of Mechanically Manipulated Multiwall Carbon Nanotube Films by Small-Angle X-ray Scattering. *J. Phys. Chem. C* **2007**, *111*, 17933–17940.
46. Bedewy, M.; Meshot, E. R.; Hart, A. J. Diameter-Dependent Kinetics of Activation and Deactivation in Carbon Nanotube Population Growth. *Carbon* **2012**, *50*, 5106–5116.

47. Meshot, E.; Bedewy, M.; Lyons, K.; Woll, A.; Juggernauth, K.; Tawfick, S.; Hart, A. Measuring the Lengthening Kinetics of Aligned Nanostructures by Spatiotemporal Correlation of Height and Orientation. *Nanoscale* **2010**, *2*, 896–900.
48. Park, S. J.; Schmidt, A. J.; Bedewy, M.; John Hart, A. Measurement of Carbon Nanotube Microstructure Relative Density by Optical Attenuation and Observation of Size-Dependent Variations. *Phys. Chem. Chem. Phys.* **2013**, *15*, 11511–11519.
49. Canny, J. A Computational Approach to Edge Detection. *IEEE Trans. Pattern Anal. Mach. Intell.* **1986**, PAMI-8, 679−698.
50. Deshpande, V. S.; Fleck, N. A. Isotropic Constitutive Models for Metallic Foams. *J. Mech. Phys. Solids* **2000**, *48*, 1253–1283.
51. Brunauer, S.; Emmett, P. H.; Teller, E. Adsorption of Gases in Multimolecular Layers. *J. Am. Chem. Soc.* **1938**, *60*, 309–319.
52. Błachnio, M.; Staszczuk, P.; Grodzicka, G. Adsorption and Porosity Properties of Pure and Modified Carbon Nanotube Surfaces. *J. Therm. Anal. Calorim.* **2008**, *94*, 641–648.
53. Jagtoyen, M.; Pardue, J.; Rantell, T.; Grulke, E.; Derbyshire, F. In *Porosity of Carbon Nanotubes, Pac. Basin Conf., Adsorpt. Sci. Technol.*; Do, D. D., Ed.; World Scientific Publishing Co. Pte. Ltd.: Singapore, Singapore, 2000; pp 289−293.
54. Shaffer, M. S. P.; Fan, X.; Windle, A. H. Dispersion and Packing of Carbon Nanotubes. *Carbon* **1998**, *36*, 1603–1612.
55. Ghasemi-Mobarakeh, L.; Semnani, D.; Morshed, M. A Novel Method for Porosity Measurement of Various Surface Layers of Nanofibers Mat using Image Analysis for Tissue Engineering Applications. *J. Appl. Polym. Sci.* **2007**, *106*, 2536–2542.
56. Bedewy, M.; Hart, A. J. Mechanical Coupling Limits the Density and Quality of Self-Organized Carbon Nanotube Growth. *Nanoscale* **2013**, *5*, 2928–2937.
57. Astrom, J. A.; Krasheninnikov, A. V.; Nordlund, K. Carbon Nanotube Mats and Fibers with Irradiation-Improved Mechanical Characteristics: A Theoretical Model. *Phys. Rev. Lett.* **2004**, *93*, 215503–1-215503-4.
58. Cox, H. L. Elasticity and Strength of Paper and Other Fibrous Materials. *Br. J. Appl. Phys.* **1952**, *3*, 72–79.
59. Berhan, L.; Yi, Y. B.; Sastry, A. M. Effect of Nanorope Waviness on The Effective Moduli of Nanotube Sheets. *J. Appl. Phys.* **2004**, *95*, 5027–5034.
60. Malik, H.; Stephenson, K. J.; Bahr, D. F.; Field, D. P. Quantitative Characterization of Carbon Nanotube Turf Topology by SEM Analysis. *J. Mater. Sci.* **2011**, *46*, 3119–3126.
61. Gao, Y.; Kodama, T.; Won, Y.; Dogbe, S.; Pan, L.; Goodson, K. E. Impact of Nanotube Density and Alignment on the Elastic Modulus Near the Top and Base Surfaces of Aligned Multi-Walled Carbon Nanotube Films. *Carbon* **2012**, *50*, 3789–3798.
62. Al-Khedher, M. A.; Pezeshki, C.; McHale, J. L.; Knorr, F. J. Quality Classification *via* Raman Identification and SEM Analysis of Carbon Nanotube Bundles Using Artificial Neural Networks. *Nanotechnology* **2007**, *18*, 355703.
63. Kim, J.-Y.; Greer, J. R. Tensile and Compressive Behavior of Gold and Molybdenum Single Crystals at the Nano-Scale. *Acta Mater.* **2009**, *57*, 5245–5253.
64. Tu, J. P.; Jiang, C. X.; Guo, S. Y.; Fu, M. F. Micro-Friction Characteristics of Aligned Carbon Nanotube Film on an Anodic Aluminum Oxide Template. *Mater. Lett.* **2004**, *58*, 1646–1649.
65. Tu, J. P.; Zhu, L. P.; Hou, K.; Guo, S. Y. Synthesis and Frictional Properties of Array Film of Amorphous Carbon Nanofibers on Anodic Aluminum Oxide. *Carbon* **2003**, *41*, 1257–1263.
66. Bhushan, B.; Xing, L.; Jungen, A.; Hierold, C. Adhesion and Friction of a Multiwalled Carbon Nanotube Sliding against Single-Walled Carbon Nanotube. *Phys. Rev. B: Condens. Matter Mater. Phys.* **2008**, *77*, 165428–1.
67. Canny, J. F. *Finding Edges and Lines in Images*; Massachusetts Institute of Technology: Cambridge, MA, **1983**.
68. Pathak, S.; Raney, J. R.; Daraio, C. Effect of Morphology on the Strain Recovery of Vertically Aligned Carbon Nanotube Arrays: An *In Situ* Study. *Carbon* **2013**, *13*, 303–316.